Dalton Transactions

ROYAL SOCIETY OF CHEMISTRY

PAPER

View Article Online
View Journal

Cite this: DOI: 10.1039/d1dt02329b

Accessing the triplet manifold of naphthalene benzimidazole–phenanthroline in rhenium(I) bichromophores†

Kaylee A. Wells, *[a] James E. Yarnell, [a,b] Sara Sheykhi, [a] Jonathan R. Palmer, [a] Daniel T. Yonemoto,[a] Rosalynd Joyce,[a] Sofia Garakyaraghi [a] and Felix N. Castellano [a]

Received 13th July 2021,
Accepted 8th August 2021

DOI: 10.1039/d1dt02329b

rsc.li/dalton

The steady-state and ultrafast to supra-nanosecond excited state dynamics of *fac*-[Re(NBI-phen)$(CO)_3$(L)](PF_6) (NBI-phen = 16H-benzo[4′,5′]isoquinolino[2′,1′:1,2]imidazo[4,5-*f*][1,10]phenanthrolin-16-one) as well as their respective models of the general molecular formula [Re(phen)$(CO)_3$(L)](PF_6) (L = PPh_3 and CH_3CN) has been investigated using transient absorption and time-gated photoluminescence spectroscopy. The **NBI-phen** containing molecules exhibited enhanced visible light absorption with respect to their models and a rapid formation (<6 ns) of the triplet ligand-centred (LC) excited state of the organic ligand, NBI-phen. These triplet states exhibit an extended excited state lifetime that enable the energized molecules to readily engage in triplet–triplet annihilation photochemistry.

Introduction

Since the original study of Wrighton and co-workers,[1] rhenium(I) carbonyl diimine (Re–CDI) molecules have remained popular due to their thermal and photochemical stability, expansive photophysical properties, and ease of synthesis.[2–9] The synthetic flexibility of this class of chromophores allows the molecules to be incorporated into polymers and supramolecular structures enabling a myriad of applications.[10–14] In fact, Re–CDI molecules are currently utilized in CO_2 reduction photochemistry, photochemical molecular devices, solar energy conversion, biological applications, and are used as sensors and photosensitizers.[15–24]

A significant drawback to many Re–CDI complexes is that they typically exhibit poor visible absorption properties and short triplet metal-to-ligand charge transfer (MLCT) lifetimes on the order of 100s of nanoseconds.[25] However, fine-tuning the electronic structure, and thus the corresponding electronic transitions, may be achieved through facile synthetic manipulations. The Re(I) dπ orbital energies are easily modified by varying the π-accepting and π-donating strengths of the ancillary ligand, which are typically associated with the HOMO energy in these complexes.[26] Additionally, the π* orbital energies, the energies of the orbitals typically associated with the LUMO energy of the chromophoric diimine ligand, may also be adjusted by adding substituents on the diimine aromatic rings.[1] Thus, modification of both the ancillary and diimine ligands causes variations in the Re(I) dπ and diimine π* orbital energies, thereby modulating the MLCT excited state properties.

Our research group has conducted numerous studies monitoring the changes in the excited state dynamics in Re–CDIs.[27–29] In these studies, we focused on appending additional organic chromophores within the ligand framework, which leads to excited state lifetime extension *via* a thermal equilibrium between the triplet ligand-centred (^{3}LC) and ^{3}MLCT excited states.[30–38] After extensively studying the photophysical interactions in these systems by modulation of both LC and MLCT excited state energies, we became interested in exploring new families of organic chromophores to determine what changes in their excited state dynamics might occur while testing their utility as light harvesters and in other potentially bespoke photophysical processes.

Most recently, we have investigated a series of thionated perinones[39] that exhibit an efficient triplet excited state formation, building off work by Anzenbacher and co-workers on oxygenated analogues.[40] Their work on polycyclic benzimidazoles inspired us to incorporate the perinone unit into rhenium(I) MLCT chromophores to increase their visible-absorption cross-sections and to determine if the perinone

[a]*Department of Chemistry, North Carolina State University, Raleigh, North Carolina, 27695-8204, USA. E-mail: fncastel@ncsu.edu*
[b]*Department of Chemistry & Chemistry Research Center, United States Air Force Academy, Colorado Springs, Colorado, 80840-6230, USA*

†Electronic supplementary information (ESI) available: Synthetic details and structural characterization data, and additional electronic theory calculations and spectroscopic data. See DOI: 10.1039/d1dt02329b

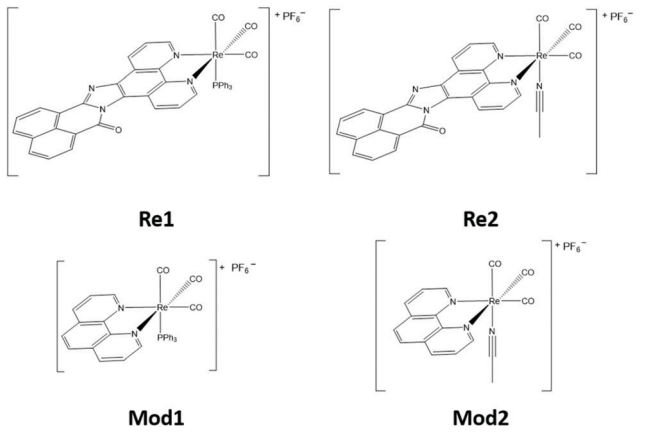

Chart 1 The bichromophores, **Re1** and **Re2**, and relevant model complexes, **Mod1** and **Mod2**, investigated here.

triplet could be sensitized through the heavy-atom effect. Perinones are polycyclic aromatic hydrocarbons that belong to a class of organic dyes that have found extensive use in the automotive industry and in organic n-type semiconductor materials.[40–44] Considering their relatively high fluorescence quantum yields and significant visible absorption cross-sections, we postulated that this class of molecules would be of interest to construct newly conceived metal–organic bichromophores. Using the synthesis method provided by Yang *et al.*[45] to synthesize a perinone that is nested within a chelating ligand, we were able to successfully synthesize and photophysically characterize two new rhenium(I) bichromophores (Chart 1), *fac*-[Re(NBI-phen)$(CO)_3(PPh_3)][(PF_6)$ (**Re1**) and *fac*-[Re (NBI-phen)$(CO)_3(CH_3CN)][(PF_6)$ (**Re2**) (NBI-phen = naphthalene benzimidazole phenanthroline) as well as two model rhenium (I) chromophores *fac*-[Re(phen)$(CO)_3(PPh_3)][(PF_6)$ (**Mod1**) and *fac*-[Re(phen)$(CO)_3(CH_3CN)][(PF_6)$ (**Mod2**) which serve as control/model molecules to make direct comparisons to the bichromophores. The CH_3CN and PPh_3 moieties were purposefully selected as strong ancillary ligands to promote the formation of ligand-centered triplet excited states. Using a combination of steady-state and time-resolved techniques supported with computational modelling, we determined that the **NBI-phen** ligand establishes the necessary energetics to serve as a visible light harvester featuring rapid formation of a long-lived ^{3}LC excited state.

Experimental

Reagents and chemicals

All reagents and chemicals were purchased from Sigma-Aldrich or VWR and used as received. All syntheses were performed under an inert nitrogen atmosphere using standard techniques for the rigorous exclusion of air and water. Spectroscopic samples were prepared using spectroscopic-grade tetrahydrofuran and were prepared under an inert and dry atmosphere of nitrogen in a glove box (MBraun). Complete synthesis and structural characterization details for all molecules investigated here are provided in the ESI.†

General techniques

All chemicals and solvents were of analytical grade, and they were used without further purification. Nuclear magnetic resonance (NMR) spectra were measured at 298 K using a Bruker® Avance NEO at 700 MHz (^{1}H) and 176 MHz (^{13}C) and were processed using MestreNova software (version 10.0.2), with the chemical shifts referenced to residual solvent signals. The chemical shifts (δ ppm) are referenced to the respective solvent, and splitting patterns are designated as s (singlet), d (doublet), t (triplet) and m (multiplet). High resolution electrospray ionization mass spectrometry (HR-ESI-MS) was performed by the Michigan State University Mass Spectrometry Core, East Lansing, MI. MS values are given as m/z. Electronic absorption spectra were measured using a Shimadzu UV-3600 and a Cary 60 UV/Vis spectrophotometer. Steady-state photoluminescence (PL) spectral and quantum yield measurements were carried out on an Edinburgh FS 5 fluorimeter equipped with an integrating sphere (absolute). Excitation scans were performed on an Edinburgh FS 920 fluorimeter. All spectral PL measurements were performed using optically dilute samples at OD $\geq$ 0.1 at the excitation wavelength.

Characterization data for studied molecules

16*H*-Benzo[4′,5′]isoquinolino[2′,1′:1,2]imidazo[4,5-*f*][1,10] phenanthrolin-16-one (NBI-phen) (64%). ^{1}H NMR (700 MHz, $CDCl_3$) δ 10.80 (d, J = 8.7 Hz, 1H), 9.56 (d, J = 8.2 Hz, 1H), 9.36 (t, J = 5.3 Hz, 2H), 9.23 (d, J = 7.4 Hz, 1H), 9.17 (d, J = 7.4 Hz, 1H), 8.66 (d, J = 8.1 Hz, 1H), 8.59 (d, J = 8.2 Hz, 1H), 8.45–8.42 (m, 1H), 8.33–8.30 (m, 1H), 8.14 (dd, J = 11.4, 4.0 Hz, 1H), 8.11 (t, J = 7.8 Hz, 1H) ppm. ^{13}C NMR (176 MHz, $CDCl_3$) δ 159.93, 151.64, 150.36, 144.93, 144.89, 139.16, 137.70, 137.44, 136.74, 135.76, 132.63, 132.25, 131.90, 129.08, 128.83, 128.02, 126.77, 126.29, 123.99, 121.76, 121.09, 120.94, 77.34, 77.16, 76.98, 21.26 ppm. MS [HR-ESI]: m/z calcd for $C_{24}H_{12}N_4OH$ $[M + H]^+$ 373.1089, found 373.1094 (Fig. S1–S3†).

***fac*-[Re(NBI-phen)$(CO)_3(PPh_3)][(PF_6)$ (Re1) (96%).** ^{1}H NMR (700 MHz, DMSO) δ 10.16 (d, J = 8.6 Hz, 1H), 9.41 (d, J = 5.0 Hz, 1H), 9.31 (t, J = 7.0 Hz, 2H), 8.97 (d, J = 7.1 Hz, 1H), 8.93 (d, J = 7.2 Hz, 1H), 8.69 (d, J = 8.0 Hz, 1H), 8.53 (d, J = 8.1 Hz, 1H), 8.09 (t, J = 7.6 Hz, 1H), 8.07–8.00 (m, 3H), 7.35 (t, J = 7.4 Hz, 3H), 7.25 (t, J = 6.7 Hz, 6H), 7.01–6.97 (m, 6H) ppm. ^{13}C NMR (176 MHz, DMSO) δ 194.95, 160.86, 155.04, 153.32, 152.42, 144.99, 144.44, 138.65, 138.32, 136.42, 134.14, 132.98, 132.86, 132.26, 132.20, 131.67, 131.05, 129.93, 129.13, 129.07, 128.08, 128.00, 127.82, 127.59, 127.50, 126.12, 125.99, 124.97, 124.47, 122.94, 122.59, 120.12, 40.02, 39.88, 39.76, 39.64, 39.52, 39.40, 39.28, 39.16 ppm. MS [HR-ESI]: m/z calcd for $C_{45}H_{27}N_4O_4PRe$ $[M]^+$ 903.1299, found 903.1307 (Fig. S4–S6†).

***fac*-[Re(NBI-phen)$(CO)_3(CH_3CN)][(PF_6)$ (Re2) (71%).** ^{1}H NMR (700 MHz, CD_3CN) δ 10.48 (d, J = 8.6 Hz, 1H), 9.51 (t, J = 5.8 Hz, 2H), 9.47 (d, J = 4.8 Hz, 1H), 9.01 (d, J = 7.2 Hz, 1H), 8.96 (d, J = 7.2 Hz, 1H), 8.57 (d, J = 8.0 Hz, 1H), 8.42 (d, J = 8.1 Hz, 1H), 8.20 (ddd, J = 18.7, 8.4, 4.9 Hz, 2H), 8.01 (dt, J = 15.5, 7.7

Hz, 2H) ppm. ^{13}C NMR (176 MHz, CD_3CN) δ 155.38, 153.88, 146.88, 140.41, 140.10, 137.58, 135.93, 134.30, 133.87, 132.96, 128.94, 128.82, 128.67, 128.11, 127.30, 127.00, 126.49, 126.28, 124.40, 123.87, 123.48, 121.29, 120.71, 118.26, 68.24, 26.20, 1.27, 1.15. MS [HR-ESI]: *m*/*z* calcd for $C_{29}H_{15}N_5O_4Re$ $[M]^+$ 682.0654, found 682.0661 (Fig. S7–S9†).

***fac*-[Re(phen)(CO)$_3$(PPh$_3$)](PF$_6$) (Mod1) (98%).** ^{1}H NMR (700 MHz, CD_3CN) δ 9.11 (dd, J = 5.1, 0.6 Hz, 2H), 8.62 (d, J = 8.2 Hz, 2H), 8.05 (s, 2H), 7.73 (dd, J = 8.2, 5.1 Hz, 2H), 7.33 (dt, J = 7.4, 3.7 Hz, 3H), 7.20 (td, J = 7.7, 2.1 Hz, 6H), 7.04–7.00 (m, 6H) ppm. ^{13}C NMR (176 MHz, CD_3CN) δ 155.79, 147.18, 140.24, 133.51, 133.45, 131.95, 131.93, 129.94, 129.88, 129.65, 129.38, 128.87, 127.56, 118.26, 1.27 ppm. MS [HR-ESI]: *m*/*z* calcd for $C_{33}H_{23}N_2O_3PRe$ $[M]^+$ 711.0976, found 711.0970 (Fig. S10–S12†).

***fac*-[Re(phen)(CO)$_3$(CH$_3$CN)](PF$_6$) (Mod2) (91%).** ^{1}H NMR (400 MHz, CD_2Cl_2) δ 9.38 (dd, J = 5.1, 1.3 Hz, 2H), 8.80 (dd, J = 8.3, 1.3 Hz, 2H), 8.21 (s, 2H), 8.05 (dd, J = 8.3, 5.1 Hz, 2H), 2.06 (s, 3H), 1.54 (s, 3H) ppm. ^{13}C NMR (176 MHz, CD_2Cl_2) δ 154.46, 147.24, 140.55, 131.72, 128.63, 127.13, 54.15, 54.00, 53.84, 53.69, 53.53, 3.70 ppm. MS [HR-ESI]: *m*/*z* calcd for $C_{17}H_{11}N_3O_3Re$ $[M]^+$ 490.0330, found 490.0339 (Fig. S13–S15†).

Ultrafast transient absorption spectroscopy

The transient absorption measurements were performed at the NCSU Imaging and Kinetic Spectroscopy (IMAKS) Laboratory using a mode-locked Ti:sapphire laser (Coherent Libra) as described previously.[46] The pump beam was directed into a parametric amplifier (Coherent OPerA Solo) to generate 400 nm excitation. The probe beam was focused onto a calcium fluoride crystal to generate a white light continuum between 350 and 750 nm. The pump beam (~700 μm) was focused and overlapped with the probe beam through a 2 mm path length cuvette to allow for a stir bar to be used. The ground-state absorption spectra were taken before and after each experiment to ensure there was no sample photodegradation during the experiment. The transient kinetic data at specific wavelengths were evaluated using the fitting routines available in OriginPro 2018b (v 9.55).

Nanosecond transient absorption and time-resolved photoluminescence spectroscopy

Nanosecond transient absorption (nsTA) and time-resolved photoluminescence (TR-PL) measurements were performed using a LP920 laser flash photolysis system from Edinburgh Instruments controlled using a L900 software program (Edinburgh Instruments). A Vibrant 355 Nd:YAG/OPO system (OPOTEK) was used for pulsed laser excitation for **Re1** and **Re2**. A Continuum Minilite Nd:YAG laser with 355 nm excitation was used for pulsed laser excitation for **Mod1** and **Mod2**. To record the transient absorption difference spectra and time-gated PL spectra in the visible portion of the spectrum, an iStar ICCD camera (Andor Technology), controlled using L900, was used. Single wavelength kinetic analysis for absorption and PL were performed using a R2658P PMT detector (Hamamatsu), which was also controlled using L900. Samples were prepared under an inert and dry atmosphere of nitrogen in a glove box (MBraun) in a 10 mm path-length quartz optical cell. Samples were prepared to have optical densities between 0.3 and 0.6 at the excitation wavelength (λ_{ex} = 410 nm for **Re1** and **Re2** and λ_{ex} = 355 nm for **Mod1** and **Mod2**). All flash-photolysis experiments were performed at room temperature unless otherwise noted. The ground-state electronic absorption spectra were recorded before and after each experiment to ensure no sample photodegradation. The transient kinetic data were evaluated using the fitting routines available in Origin Student 2018b (v. 9.55).

Density functional theory (DFT) and time-dependent DFT (TD-DFT) calculations

Density functional theory (DFT) and time-dependent DFT (TD-DFT) calculations were performed on all complexes using the Gaussian 16 software package (revision A.03)[47] and the computational resources of the North Carolina State University High Performance Computing Center. Geometry optimizations and TD-DFT calculations were performed using the PBE1PBE (PBE0) functional[48] and the Def2-SVP basis set of the Alrichs group on all atoms.[49] The Stuttgart–Dresden effective core potentials (ECP) were used to replace the core electrons in rhenium for all calculations.[50] The polarizable continuum model (PCM)[51] was used to simulate the effects of the tetrahydrofuran (THF) solvent environment for all calculations, and the GD3 dispersion correction[52] was used for all ground and excited state geometry optimizations. Frequency calculations were performed on all optimized structures and no imaginary frequencies were obtained. TD-DFT calculations were used to obtain the energy, oscillator strength, and related molecular orbital contributions for the 50 lowest singlet–singlet vertical transitions for all the molecules studied. The natural transition orbitals (NTOs)[53] of the low-lying singlet–singlet transitions were generated and visualized using GaussView 6.0.[54] Triplet spin density surfaces and natural orbitals (NOs) were generated from the optimized T_1 excited states and were also visualized using GaussView 6.0.

Results and discussion

Syntheses

All syntheses were performed under an inert and dry nitrogen atmosphere using standard techniques. All reagents were purchased from VWR or Sigma-Aldrich and used as received. The synthetic procedures used to make all the chromophores are outlined in Scheme 1. The identity and purity of all compounds studied were confirmed using ^{1}H NMR, ^{13}C NMR, and high-resolution mass spectrometry. Synthetic details for all precursors and products in this study are included in the ESI.† Briefly, 1,8-naphthalic anhydride, 5,6-diamino-1,10-phenanthroline, and acetic acid were added to a pressure vessel and heated to 140 °C for 24 hours to synthesize the **NBI-phen** ligand.[45] Synthesis of **Re1** and **Re2** began with **NBI-phen** and $Re(CO)_5Cl$ refluxing in toluene to obtain the chloride intermediate. **Re1** was then treated with AgOTf in EtOH to remove the chloride,

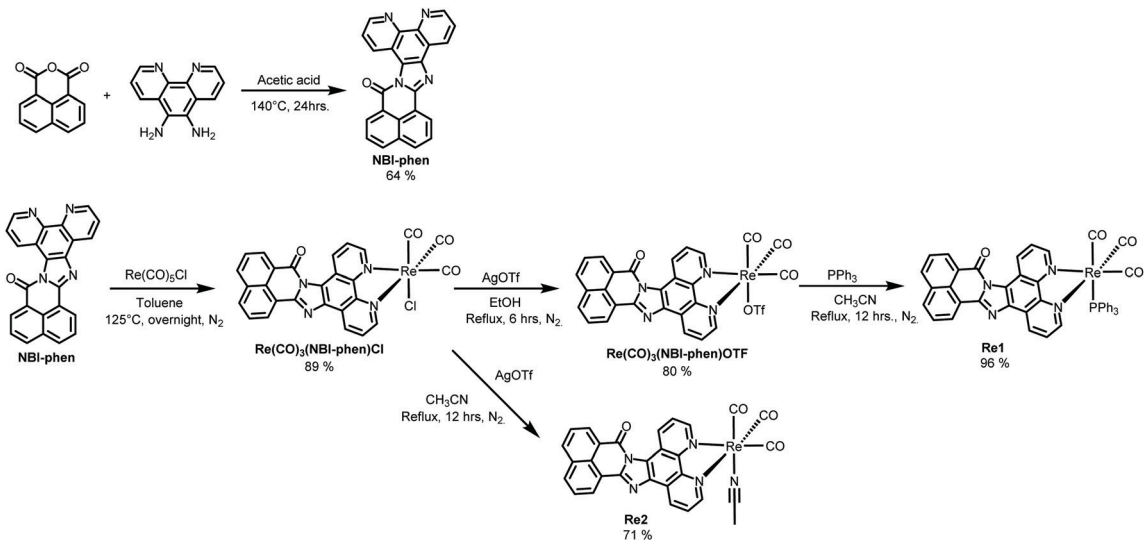

Scheme 1 Synthetic pathways leading to **NBI-phen**, **Re1**, and **Re2**.

which was then reacted with PPh_3 in CH_3CN to synthesize the final product. Synthesis of **Re2** also began with the chloride intermediate as with **Re1**, but was treated with AgOTf in CH_3CN to synthesize the final product. **Mod1** and **Mod2** were synthesized according to previous literature precedence.[55,56]

Electronic structure calculations

Ground state geometry optimizations were initially performed on both the model complexes (**Mod1** and **Mod2**) and the bichromophores (**Re1** and **Re2**) to establish how the frontier molecular orbitals are altered by interchanging 1,10-phenanthroline with **NBI-phen** as the diimine ligand. Representative frontier orbital diagrams are shown in Fig. 1 for **Mod1** and **Re1**. Corresponding diagrams are shown in Fig. S16† for **Mod2** and **Re2**. The frontier orbitals for **Mod1** depict the three highest occupied molecular orbitals to be the Re(I) dπ orbitals, while the LUMO corresponds to the π* orbital on the diimine. This suggests that the lowest energy transitions in the UV-Vis region of this complex are MLCT in nature. Similar conclusions can be drawn from Fig. S16† for **Mod2**. Conversely, the frontier orbitals for **Re1** reveal the emergence of a diimine-based π molecular orbital as the HOMO, while the LUMO is

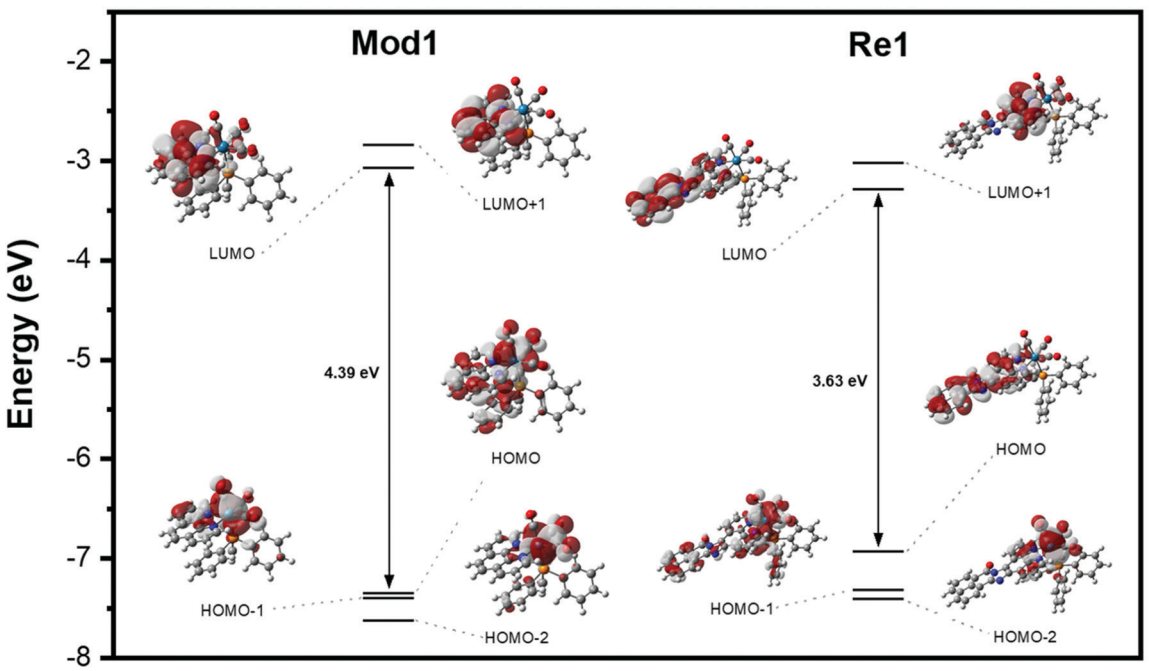

Fig. 1 Representative frontier molecular orbital diagrams of **Mod1** and the corresponding NBI–phen complex **Re1**, where L = PPh_3.

lowered in energy and maintained as the π* orbital on the diimine. Additionally, the HOMO–LUMO gap is calculated to be much smaller in **Re1** than in **Mod1** (~0.6 eV). As a result, it is expected that the lowest energy transition in **Re1** is ligand-centered and that the complex will exhibit superior visible light absorption than its corresponding model complex, **Mod1**. Similarly, this trend is also observed when comparing **Mod2** to **Re2**.

Using the optimized ground state geometries, the electronic absorption spectrum of each complex was simulated by calculating the 50 lowest singlet transitions for each complex. The calculated electronic absorption spectra of **Mod1** and **Re1** are presented in Fig. S17 and S18,† respectively, and are overlaid with their experimental spectra. For **Mod1**, the calculated spectrum is in good agreement with the experimental data, with the lowest energy absorption maximum being slightly overestimated in energy. The calculated electronic absorption spectrum of **Re1** is also in good agreement with the experimental data, with the lowest energy absorption maximum being slightly underestimated in energy. Natural transition orbitals were calculated for the three lowest-lying vertical excitations of **Mod1** and **Re1** to elucidate the characteristics of the transitions making up the majority of the lowest energy absorption bands. The resultant hole–particle pairs are shown in Fig. S21 for **Mod1** and in Fig. S22 for **Re1**.† The energies and oscillator strengths for these transitions are compiled in Table S1.† The three lowest energy singlet transitions for **Mod1** are all MLCT in nature with a low oscillator strength. The hole corresponds to a Re(I) dπ orbital in each case and the particle corresponds to a π* orbital on the diimine. Conversely, the lowest energy singlet transition for **Re1** is LC in nature with a significant oscillator strength. The hole corresponds to a π orbital on the diimine and the particle corresponds to a π* orbital on the diimine. The pure MLCT transition for **Re1** is not observed until the $S_0 \rightarrow S_3$ transition occurs, which is significantly higher in energy with much lower oscillator strength than the LC transition (see Table S1†). These results are consistent with those predicted from the change in frontier molecular orbitals shown in Fig. 1 when interchanging 1,10-phenanthroline with **NBI-phen** as the diimine, and is also observed in **Mod2** and **Re2** (Fig. S23 and S24†).

The characteristics of the lowest energy triplet excited state in the bichromophores were assigned by calculating the natural orbitals from the optimized geometry of the lowest energy triplet state. Using **Re1** as a representative example, the singly occupied natural orbitals display the unpaired spins to be located on the diimine ligand in the orbitals of π-symmetry (Fig. S25†). It should be noted that the natural orbitals depict a significant degree of intra-ligand charge transfer in this triplet excited state, which is not observed in the lowest energy singlet vertical LC transition predicted using TD-DFT. Additionally, the Re(I) dπ natural orbitals are all observed to be doubly occupied, further confirming there is no MLCT character in this lowest energy triplet excited state. The natural orbital analysis for **Re2** depicted in Fig. S26† gives the same results. Finally, the spin density surfaces generated from the lowest energy triplet states of **Re1** and **Re2** both depict spin density to be localized solely on the **NBI-phen** ligand (Fig. S27†), corroborating that the lowest energy triplet excited states in these complexes are ^{3}LC.

Electronic absorption and photoluminescence spectroscopy

The electronic absorption spectra of **Re1–2** and **Mod1–2** are presented in Fig. 2, with additional spectroscopic results shown in Table 1. **Mod1** and **Mod2** are the model inorganic chromophores for this study and **NBI** (Fig. S29†) is used as a model organic chromophore. **NBI-phen** is not used as the organic model due to its insolubility in many organic solvents. During a photophysical study of the two bichromophores (discussed below), **Re1** and **Re2**, it became clear that these molecules shared remarkably similar characteristics to the features seen in an Ir(III) chromophore featuring the **NBI** ligand.[57] While the photophysical data for **NBI** will be used in lieu of **NBI-phen**, it is important to note that due to the extended π system of **NBI-phen** a bathochromic shift in its absorption and photoluminescence features is expected.

From Fig. 2A, the visible absorption cross-section was observed to be markedly enhanced for **Re1** and **Re2** as compared to their respective model chromophores, Fig. 2B. This increase in visible light absorptivity is a direct consequence of the **NBI** being fused to the 1,10-phenanthroline ligand. The higher energy transitions of both **Re1** and **Re2** in the UV region, <300 nm, are of higher energy π → π* transitions on the diimine ligand. The generally broad and slightly featured low energy band has a peak maximum at 406 nm with a shoulder at 425 nm for **Re1** and at 404 nm with a shoulder at 425 nm for **Re2**. The TD-DFT calculations of both **Re1** and **Re2**

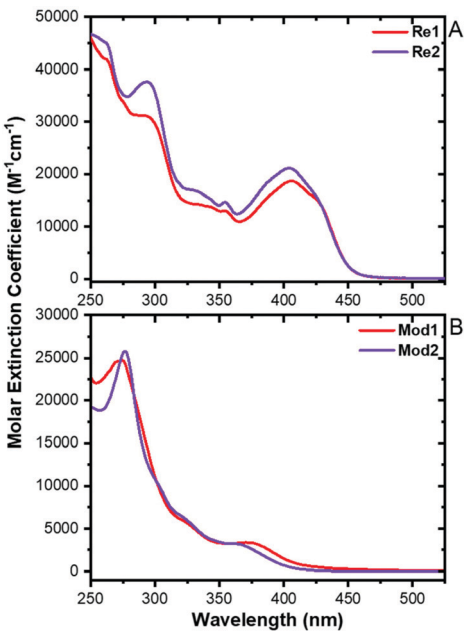

Fig. 2 Electronic absorption spectra of (A) **Re1** and **Re2** and (B) **Mod1** and **Mod2** measured in THF.

Table 1 Electronic absorbance and photoluminescence data of studied molecules in THF

Molecule	λ_{abs}, nm (ε, M^{-1} cm^{-1})	λ_{am}, nm RT[a] (77 K)[b]	Φ_{em} [c] (%)
Re1	292 (31 200) 406 (18 700)	535, 624, 688 (540, 614, 675)	<1
Re2	294 (37 700) 404 (21 200)	506, 633, 689 (532, 615, 672)	<1
Mod1	275 (24 700) 374 (3340)	524	46.8
Mod2	277 (25 800) 365 (3180)	548	11.7

[a] Room temperature PL maxima are corrected, and they have been recorded in deaerated THF. [b] 77 K measurements have been carried out using 2-MeTHF, and PL maxima are uncorrected. [c] Absolute quantum yields.

indicate the lowest energy transition, $S_0 \rightarrow S_1$, is a $\pi \rightarrow \pi^*$ transition localized on **NBI-phen**. It is not until the $S_0 \rightarrow S_3$ transition that MLCT character is observed at a much higher energy. **NBI**, Fig. S29,† has a largely broad and featureless low energy band. Computations show that the two lowest energy transitions are composed of a charge transfer band where the electron density is localized along the π system of the entire ligand and then shifts towards the naphthalene end of the ligand ($S_0 \rightarrow S_1$) and a $\pi \rightarrow \pi^*$ transition ($S_0 \rightarrow S_2$).[39] This behaviour is mirrored in the **NBI-phen** ligand as seen in the computations (Fig. S28†).

The static PL spectra of **Re1** and **Re2** share similar features (Fig. 3A) after being excited at 415 nm. **Re1** has three peak maxima, *i.e.*, at 535, 624, and 688 nm. The peak maxima of **Re2** are 506, 633, and 689 nm. The slight shoulder at 477 nm in both complexes is from the Raman band of THF, which is noticeable due to the low quantum yield values for both the bichromophoric complexes (<1%). For both the molecules, the highest energy peak is assigned to the singlet fluorescence of the organic chromophore due to their similar peak positions and because the peak remains even after being exposed to molecular dioxygen (Fig. S30†). The two lower energy features are therefore designated to be the triplet PL emission of the **NBI-phen** ligand, which was completely quenched by the exposure to molecular dioxygen (Fig. S30†). Further evidence of the triplet character of these peaks is the triplet sensitized spectrum of **NBI** recorded by Yarnell and co-workers.[57] In their study, they found the triplet state of **NBI** to emit at 607 and 664 nm in 2-MeTHF. Excitation scans (Fig. S31†) monitoring emission intensity at all three observed PL peaks for both **Re1** and **Re2** reproduced the lowest energy band of the absorbance spectra that we characterize as exclusively **NBI-phen** electronic transitions. All these data combined suggest that these molecules obey Kasha's rule: the lowest emitting state of these two bichromophores consists of triplet **NBI-phen** with residual singlet fluorescence of the same unit.

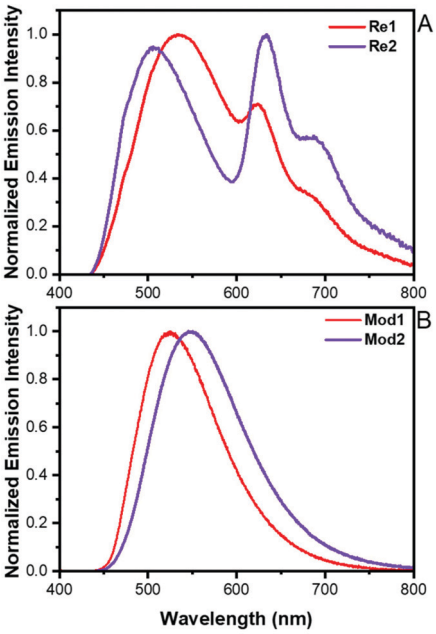

Fig. 3 Static photoluminescence spectra of (A) **Re1** and **Re2** (λ_{ex} = 415 nm) and (B) **Mod1** and **Mod2** (λ_{ex} = 355 nm) in deaerated THF.

Mod1 and **Mod2** electronic absorption spectra are presented in Fig. 2B and their steady-state PL in Fig. 3B. The absorbance and photoluminescence spectra of both model compounds are analogous to previously synthesized rhenium (I) tricarbonyl diimines of a similar structure.[2,28,29,55,56,58] **Mod1** and **Mod2** absorption spectra are characterized by strong UV absorption <300 nm correlating to $\pi \rightarrow \pi^*$ transitions of the phenanthroline ligand. The lower energy bands of the model complexes with peak maxima at 374 and 365 nm for **Mod1** and **Mod2**, respectively, are attributed to the MLCT transition, consistent with previously reported data of similarly constructed molecules and agree with the TD-DFT calculations performed (discussed above). The PL of both models (Fig. 3B) is assigned to the ^{3}MLCT excited state due to their large Stokes shift (524 nm, **Mod1**, and 548 nm, **Mod2**), broad and featureless profile, and excited state lifetime (discussed below). Additionally, previous molecules of a similar structural motif have their PL assigned to ^{3}MLCT character.[2,28,29,55,56,58]

Transient absorption and time-resolved PL spectroscopy

Ultrafast transient absorption spectroscopy. The ultrafast excited state absorption difference spectra of **Re2** are presented in Fig. 4A, and those of **Mod2** in Fig. 5A, while those of **Re1** and **Mod1** are presented in Fig. S32A and S38A,† respectively. **Re2** ultrafast excited state difference spectra (Fig. 4A) are used as representative data for both bichromophores as the UFTA of **Re1** is nearly identical. The UFTA of **Re2** shares similar features at early time scales with **NBI** (Fig. S37†). The prompt signal shows that there are excited state features that align well

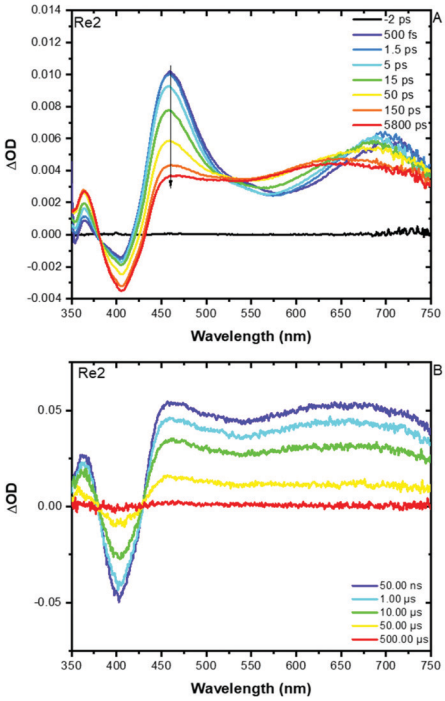

Fig. 4 UFTA of (A) **Re2** in THF following 400 nm pulsed laser excitation (105 fs FWHM, 0.3 mJ per pulse) and (B) nsTA of **Re2** in deaerated THF following 415 nm excitation (1.8 mJ per pulse).

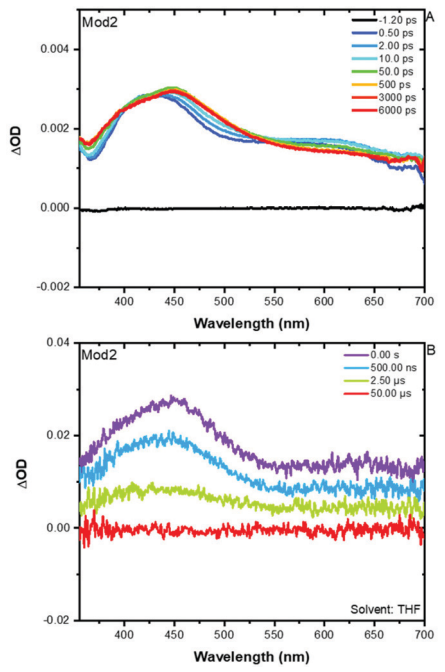

Fig. 5 Representative (**Mod1** and **Mod2**) transient absorption spectra of (A) UFTA of **Mod2** following 350 nm excitation (105 fs FWHM, 50 µJ per pulse) in THF and (B) nsTA of **Mod2** following 355 nm excitation (1.8 mJ per pulse) in deaerated THF.

with **NBI** at 363, 460, and 698 nm. The dip in the excited state between 460 and 698 nm is due to stimulated emission that is not quite intense enough to be a negative feature but still distorts the excited state features at early time delays. Additionally, there is a ground state bleach centered at 406 nm, in good agreement with the low energy absorption band already assigned to ^{1}LC transitions within the **NBI-phen** unit (Fig. 2A). Over the course of the experiment, the excited state features evolve into a state where there is no stimulated emission; the excited state features in the visible region peak at 460 nm and span out into the NIR region. This behaviour is in stark contrast to **NBI** where no new features are seen after 6 ns (Fig. S37†).

Single wavelength analysis of **Re2** at 460 nm yields a biexponential decay where the first time constant is 10.5 ps and the second time constant is 74.2 ps (**Re1** τ_1 = 7.6 and τ_2 = 39.1 ps) (Fig. S33 and S34†). Due to the similar features between the prompt signal of the bichromophores and the **NBI**, we have attributed the first time constant to the singlet decay of the organic ligand on the bichromophores. We have assigned the second time constant to the ISC rate from the singlet manifold to the triplet manifold of the **NBI-phen** ligand. These two time constants are consistent with the work by Blanco-Rodríguez *et al.*, where ISC from the singlet state to the triplet state is possible due to the close proximity of a heavy atom, rhenium.[59,60] There is no spectroscopic or kinetic evidence that the MLCT-based electronic transitions play an active role in the ultrafast time domain of these molecules as seen in previous bichromophoric studies. However, there is spectroscopic evidence that **NBI-phen** enters its triplet excited state. The final trace at 6 ns in Fig. 4A mimics the initial trace in the nsTA spectra in Fig. 4B. Lack of new spectroscopic features between the two experiments implies that the final excited state is formed in the ultrafast time regime and then decays back to the ground state. Further evidence that supports the assignment of ^{3}LC character of **NBI-phen** as the final excited state is discussed immediately below.

Representative ultrafast excited state difference spectra of the models are of **Mod2** and are presented in Fig. 5A (**Mod1**, Fig. S38A†). After 350 nm excitation (105 fs FWHM, 50 µJ per pulse), the compound displays only excited state features that it develops a more refined shape over the course of the experiment with peak maxima at 400 and 450 nm. These absorption features are vastly different from their respective bichromophoric molecules (Fig. 4A and S32A†). The associated short time constants observed in **Mod1** and **Mod2** are significantly different (<150 fs) from those measured in **Re1** and **Re2**. Additionally, the longer time decay components observed in the model complexes, 8.84 and 9.35 ps for **Mod2** and **Mod1**, respectively (Fig. S39 and S40†), are unique with respect to the kinetics observed in the title chromophores. The faster time constant measured for both models is assigned to intersystem crossing and formation of the radical anion on the diimine ligand. The longer time components are believed to correspond to vibrational cooling on the triplet surface. Both time constants are in good agreement with previously studied Re–CDI molecules featuring MLCT excited states.[5,8,28,29]

Nanosecond transient absorption and time-gated PL. The nsTA excited state difference spectra of **Re2** are shown in Fig. 4B as representative data for both bichromophores of this study. From the trace, we see that the features are consistent with the final trace from the UFTA data, indicating that the same excited state is observed at the end of the UFTA experiment and throughout the nsTA experiment. There are two excited state features, one in the UV region *ca.* 375 nm, and one that peaks in the visible region near 460 nm, which then broadens out to the NIR region. These two features sandwich a ground state bleach at 400 nm. Because both **Re1** and **Re2** have nearly identical excited state features and ground state bleaches, this suggests that the excited state observed in the ns time domain is of ^{3}**NBI-phen** as it is the shared ligand between the two compounds. Additionally, these features persist for hundreds of microseconds, suggesting that the associated excited state observed is of ^{3}LC character. Further evidence support that the excited state observed is ^{3}**NBI-phen**, which is the triplet sensitized nsTA spectrum of ^{3}**NBI** presented by Yarnell *et al.*, where there is an excited state feature *ca.* 450 nm, which spans out to the NIR region.[57] This slight blue shift in the excited state difference spectrum is expected as the ligand is structured differently and is a free ligand in solution. Single wavelength kinetic analysis at 460 nm revealed a kinetic trace that could not be fit to a monoexponential decay and was found to be power-dependent in nature. Observing this phenomenon, we fit the data using eqn (1):

$$\Delta A = \frac{\Delta A_0(1-\beta)}{\exp(k_T t) - \beta} \quad (1)$$

where β equates to the initial fraction of triplet decay occurring through TTA.[61]

From this fitting equation and multiple experimental pulse energies (Fig. S35 and S36, Tables S3 and S4†), we were able to ascertain that these molecules, **Re1** and **Re2**, undergo triplet–triplet annihilation (TTA) with themselves and have an experimental triplet decay rate constant on the order of 10^3 s^{-1}.

Room temperature and 77 K TR PL spectra of **Re2** are shown in Fig. 6 with relevant peak maxima shown in Table 1. In the RT experiment (Fig. 6A) with a long gate (10.00 μs), we were able to resolve one feature at 515 nm with two red shoulders at 623 and 684 nm. Under similar experimental conditions, **Re1** displayed a feature at 532 nm, but only one shoulder at 622 nm (Fig. S41A†). In a frozen glass at 77 K, the red features became more pronounced, appearing much more like the features seen in the static PL spectra (Fig. 3A). As such, we confidently assigned the features as ^{1}LC and ^{3}LC in nature. Additionally, we were able to watch the RT PL decay over the same time range as the transient absorption (Fig. 4B) experiment discussed above. The incredibly long-lived excited state, excited state spectral features, TR PL, and calculations all lend significant support in assigning ^{3}**NBI-phen** as the final excited state.

Mod2 nsTA is shown in Fig. 5B and is a representative of **Mod1** (Fig. S38B†). At 355 nm excitation, a prompt signal shows positive absorption features across the entire visible region, similar to its UFTA, Fig. 5A. The excited state features of both model complexes resemble the ^{3}MLCT transition in Re–CDI molecules, featuring a phenanthroline ligand.[27–29,62] Additionally, the lifetimes of the two models are consistent with $[Re(phen)(CO)_3(L)]^+$ (L = neutral ligand) molecules featuring a ^{3}MLCT with lifetimes of 2.2 and 2.3 μs for **Mod1** and **Mod2**, respectively (Fig. S44 and S45†).[2,28,56] The TR PL and PL lifetimes of both models are presented in Fig. S42–S45.† Like their steady-state PL, the TR PL spectra of the models are broad and featureless with peak maxima at 516 nm and 540 nm for **Mod1** and **Mod2**, respectively. Over the course of the experiment, no new features are noted, and the experimental lifetime of their PL (τ = 2.5 μs for both **Mod1** and **Mod2**) matches their nsTA lifetime, indicating that the final excited state is also the emitting state.

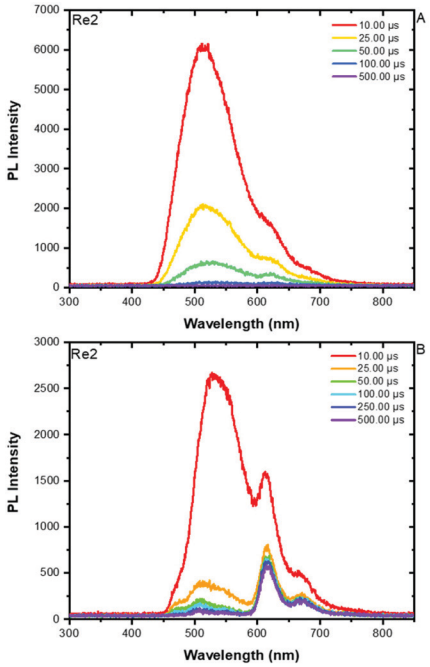

Fig. 6 Representative (**Re1** and **Re2**) time-resolved photoluminescence data of **Re2** at (A) room temperature in deaerated THF and at (B) 77 K in 2-MeTHF following 415 nm excitation (1.8 mJ per pulse).

Conclusions

In this study, we have successfully integrated a perinone, **NBI-phen**, onto two Re(I) carbonyl diimine complexes and have fully characterized the excited state processes from prompt excitation to ground state and compared them to their respective model compounds. Additionally, we have used electronic structure calculations to provide theoretical relevance and support for our experimental findings. This study has revealed that by integrating the **NBI-phen** ligand into the framework of Re–CDI complexes, we obtain higher visible light absorptivity and extended excited state lifetimes that are capable of self-

quenching *via* TTA in solution. However, the incorporation of perinone onto the Re(I) centre dramatically decreased the quantum yield. We conclude that upon excitation, the ^{1}LC band of **NBI-phen** undergoes ISC to the ^{3}LC due to the heavy-atom effect presented by Re(I), where it then decays back to the ground state. Lastly, while a thermal equilibrium between the organic ligand and the Re–CDI complex was not formed in these two systems due to the large energy gap between the ^{3}MLCT and ^{3}LC states, the long-lived nature of the **NBI-phen** ^{3}LC state makes these materials an ideal candidate as a low-lying triplet reservoir. As such, if an inorganic chromophore of appropriate MLCT energy is introduced in place of our present Re–CDI complexes, a strong thermal equilibrium is likely to establish.[27–38] However, these materials are well suited for light harvesting applications, and readily sensitize the organic triplet, making them good candidates for a variety of applications.[11,13,15–17,24]

Author contributions

KAW was involved in conceptualization, formal analysis, experimental investigation, validation, visualization, and writing and editing the manuscript. JEY was involved in conceptualization and experimental investigation. SS was involved in experimental investigation and writing the original manuscript. JRP was involved in experimental investigation and editing the manuscript. DTY was involved in validation and editing the manuscript. RJ was involved in experimental investigation. SG was involved in experimental investigation. FNC was involved in conceptualization, funding acquisition, resources, visualization, and editing the manuscript.

Conflicts of interest

There are no conflicts of interest to declare.

Acknowledgements

This work was supported by the U.S. Department of Energy, Office of Science, Office of Basic Energy Sciences, under Award No. DE-SC0011979. Some personnel were supported by the National Science Foundation (CHE-1955795, K. A. W.), the Air Force Institute of Technology (AFIT, J. E. Y.), and the Air Force Office of Scientific Research (FA9550-18-1-0331, D. T. Y.).

References

1 M. Wrighton and D. L. Morse, *J. Am. Chem. Soc.*, 1974, **96**, 998–1003.
2 L. Wallace and D. P. Rillema, *Inorg. Chem.*, 1993, **32**, 3836–3843.
3 S. A. Moya, J. Guerrero, R. Pastene, R. Sartori, R. Schmidt, R. Sariego, J. Sanz-Aparicio, I. Fonseca and M. Martinez-Ripoll, *Inorg. Chem.*, 1994, **33**, 2341–2346.
4 G. E. Shillito, T. B. J. Hall, D. Preston, P. Traber, L. Wu, K. E. A. Reynolds, R. Horvath, X. Z. Sun, N. T. Lucas, J. D. Crowley, M. W. George, S. Kupfer and K. C. Gordon, *J. Am. Chem. Soc.*, 2018, **140**, 4534–4542.
5 A. El Nahhas, C. Consani, A. M. Blanco-Rodríguez, K. M. Lancaster, O. Braem, A. Cannizzo, M. Towrie, I. P. Clark, S. Záliš, M. Chergui and A. Vlček, *Inorg. Chem.*, 2011, **50**, 2932–2943.
6 J. M. Villegas, S. R. Stoyanov, W. Huang and D. P. Rillema, *Inorg. Chem.*, 2005, **44**, 2297–2309.
7 J. L. Smithback, J. B. Helms, E. Schutte, S. M. Woessner and B. P. Sullivan, *Inorg. Chem.*, 2006, **45**, 2163–2174.
8 H. Atallah, C. M. Taliaferro, K. A. Wells and F. N. Castellano, *Dalton Trans.*, 2020, **49**, 11565–11576.
9 A. Vlček, in *Photophysics of Organometallics*, ed. A. J. Lees, Springer Berlin Heidelberg, Berlin, Heidelberg, 2010, pp. 115–158, DOI: 10.1007/3418_2009_4.
10 A. J. North, J. A. Karas, M. T. Ma, P. J. Blower, U. Ackermann, J. M. White and P. S. Donnelly, *Inorg. Chem.*, 2017, **56**, 9725–9741.
11 N. M. Orchanian, L. E. Hong, J. A. Skrainka, J. A. Esterhuizen, D. A. Popov and S. C. Marinescu, *ACS Appl. Energy Mater.*, 2019, **2**, 110–123.
12 M. A. Shestopalov, Y. V. Mironov, K. A. Brylev, S. G. Kozlova, V. E. Fedorov, H. Spies, H.-J. Pietzsch, H. Stephan, G. Geipel and G. Bernhard, *J. Am. Chem. Soc.*, 2007, **129**, 3714–3721.
13 M. Toganoh, S. Ikeda and H. Furuta, *Inorg. Chem.*, 2007, **46**, 10003–10015.
14 O. A. Nikonova, K. Jansson, V. G. Kessler, M. Sundberg, A. I. Baranov, A. V. Shevelkov, D. V. Drobot and G. A. Seisenbaeva, *Inorg. Chem.*, 2008, **47**, 1295–1300.
15 F. Franco, C. Cometto, C. Garino, C. Minero, F. Sordello, C. Nervi and R. Gobetto, *Eur. J. Inorg. Chem.*, 2015, **2015**, 296–304.
16 J. Agarwal, E. Fujita, H. F. Schaefer and J. T. Muckerman, *J. Am. Chem. Soc.*, 2012, **134**, 5180–5186.
17 H. Takeda, K. Koike, H. Inoue and O. Ishitani, *J. Am. Chem. Soc.*, 2008, **130**, 2023–2031.
18 K. P. S. Zanoni and N. Y. Murakami Iha, *Dalton Trans.*, 2017, **46**, 9951–9958.
19 A. O. T. Patrocinio, K. P. M. Frin and N. Y. Murakami Iha, *Inorg. Chem.*, 2013, **52**, 5889–5896.
20 K. M. Knopf, B. L. Murphy, S. N. MacMillan, J. M. Baskin, M. P. Barr, E. Boros and J. J. Wilson, *J. Am. Chem. Soc.*, 2017, **139**, 14302–14314.
21 M. A. Klenner, B. Zhang, G. Ciancaleoni, J. K. Howard, H. E. Maynard-Casely, J. K. Clegg, M. Massi, B. H. Fraser and G. Pascali, *RSC Adv.*, 2020, **10**, 8853–8865.
22 L. C.-C. Lee, K.-K. Leung and K. K.-W. Lo, *Dalton Trans.*, 2017, **46**, 16357–16380.
23 J. R. Dilworth and S. J. Parrott, *Chem. Soc. Rev.*, 1998, **27**, 43–55.
24 N. Manav, P. E. Kesavan, M. Ishida, S. Mori, Y. Yasutake, S. Fukatsu, H. Furuta and I. Gupta, *Dalton Trans.*, 2019, **48**, 2467–2478.

25 V. Balzani, S. Campagna, A. Barbieri and I. Ebrary, *Photochemistry and Photophysics of Coordination Compounds II*, Springer-Verlag, Berlin, Germany, 2007.
26 J. V. Caspar, E. M. Kober, B. P. Sullivan and T. J. Meyer, *J. Am. Chem. Soc.*, 1982, **104**, 630–632.
27 J. E. Yarnell, J. C. Deaton, C. E. McCusker and F. N. Castellano, *Inorg. Chem.*, 2011, **50**, 7820–7830.
28 K. A. Wells, J. E. Yarnell, J. R. Palmer, T. S. Lee, C. M. Papa and F. N. Castellano, *Inorg. Chem.*, 2020, **59**, 8259–8271.
29 J. E. Yarnell, K. A. Wells, J. R. Palmer, J. M. Breaux and F. N. Castellano, *J. Phys. Chem. B*, 2019, **123**, 7611–7627.
30 D. S. Tyson, J. Bialecki and F. N. Castellano, *Chem. Commun.*, 2000, 2355–2356.
31 F. N. Castellano, *Acc. Chem. Res.*, 2015, **48**, 828–839.
32 F. N. Castellano, *Dalton Trans.*, 2012, **41**, 8493.
33 D. S. Tyson and F. N. Castellano, *J. Phys. Chem. A*, 1999, **103**, 10955–10960.
34 D. S. Tyson, K. B. Henbest, J. Bialecki and F. N. Castellano, *J. Phys. Chem. A*, 2001, **105**, 8154–8161.
35 C. E. McCusker, A. Chakraborty and F. N. Castellano, *J. Phys. Chem. A*, 2014, **118**, 10391–10399.
36 J. E. Yarnell, C. E. McCusker, A. J. Leeds, J. M. Breaux and F. N. Castellano, *Eur. J. Inorg. Chem.*, 2016, **2016**, 1808–1818.
37 D. S. Tyson, C. R. Luman, X. Zhou and F. N. Castellano, *Inorg. Chem.*, 2001, **40**, 4063–4071.
38 D. T. Yonemoto, C. M. Papa, C. Mongin and F. N. Castellano, *J. Am. Chem. Soc.*, 2020, **142**, 10883–10893.
39 J. R. Palmer, K. A. Wells, J. E. Yarnell, J. M. Favale and F. N. Castellano, *J. Phys. Chem. Lett.*, 2020, **11**, 5092–5099.
40 M. Mamada, C. Pérez-Bolívar, D. Kumaki, N. A. Esipenko, S. Tokito and P. Anzenbacher Jr., *Chem. – Eur. J.*, 2014, **20**, 11835–11846.
41 J. Mizuguchi, *J. Phys. Chem. B*, 2004, **108**, 8926–8930.
42 M. G. Debije, P. P. C. Verbunt, P. J. Nadkarni, S. Velate, K. Bhaumik, S. Nedumbamana, B. C. Rowan, B. S. Richards and T. L. Hoeks, *Appl. Opt.*, 2011, **50**, 163–169.
43 K. I. Kobrakov, N. S. Zubkova, G. S. Stankevich, Y. S. Shestakova, V. S. Stroganov and O. I. Adrov, *Fibre Chem.*, 2006, **38**, 183–187.
44 R. O. Loutfy, A. M. Hor, P. M. Kazmaier, R. A. Burt and G. K. Hamer, *Dyes Pigm.*, 1991, **15**, 139–156.
45 Y. Yang, J. Brückmann, W. Frey, S. Rau, M. Karnahl and S. Tschierlei, *Chem. – Eur. J.*, 2020, 17027–17034.
46 S. Garakyaraghi, E. O. Danilov, C. E. McCusker and F. N. Castellano, *J. Phys. Chem. A*, 2015, **119**, 3181–3193.
47 M. J. Frisch, G. W. Trucks, H. B. Schlegel, G. E. Scuseria, M. A. Robb, J. R. Cheeseman, G. Scalmani, V. Barone, G. A. Petersson, H. Nakatsuji, *et al.*, *Gaussian 16, Revision A.03*, 2016.
48 C. Adamo and V. Barone, *J. Chem. Phys.*, 1999, **110**, 6158–6170.
49 F. Weigend and R. Ahlrichs, *Phys. Chem. Chem. Phys.*, 2005, **7**, 3297–3305.
50 D. Andrae, U. Häußermann, M. Dolg, H. Stoll and H. Preuß, *Theor. Chim. Acta*, 1990, **77**, 123–141.
51 M. Cossi, G. Scalmani, N. Rega and V. Barone, *J. Chem. Phys.*, 2002, **117**, 43.
52 S. Grimme, J. Antony, S. Ehrlich and H. Krieg, *J. Chem. Phys.*, 2010, **132**, 154104.
53 R. L. Martin, *J. Chem. Phys.*, 2003, **118**, 4775–4777.
54 R. Dennington, T. A. Keith and J. M. Millam, *Gauss View, Ver. 6*, 2016.
55 J. V. Caspar and T. J. Meyer, *J. Phys. Chem.*, 1983, **87**, 952–957.
56 M. R. Gonçalves and K. P. M. Frin, *Polyhedron*, 2017, 20–27.
57 J. E. Yarnell, P. De La Torre and F. N. Castellano, *Eur. J. Inorg. Chem.*, 2017, **2017**, 5238–5245.
58 I. Chakraborty, J. Jimenez, W. M. C. Sameera, M. Kato and P. K. Mascharak, *Inorg. Chem.*, 2017, **56**, 2863–2873.
59 A. D. McNaught and A. Wilkinson, *IUPAC Compendium of Chemical Terminology "Gold Book"*, Blackwell Scientific Publications, Oxford, 2nd edn, 1997.
60 A. M. Blanco-Rodríguez, H. Kvapilová, J. Sýkora, M. Towrie, C. Nervi, G. Volpi, S. Záliš and A. Vlček, *J. Am. Chem. Soc.*, 2014, **136**, 5963–5973.
61 F. Deng, J. Blumhoff and F. N. Castellano, *J. Phys. Chem. A*, 2013, **117**, 4412–4419.
62 K. Kalyanasundaram, *J. Chem. Soc., Faraday Trans. 2*, 1986, **82**, 2401.

